Interface Coupling as a Crucial Factor for Spatial Localization of Electronic States in a Heterojunction of Graphene Nanoribbons

Yawei Lv,[1,2] Qijun Huang,[1] Sheng Chang,[1,*] Hao Wang,[1] Jin He,[1] Chun Wei,[3] Anqi Liu,[1] Shizhuo Ye,[1] and Wei Wang[1]

[1]*Key Laboratory of Artificial Micro- and Nano-Structures of Ministry of Education, School of Physics and Technology, Wuhan University, Wuhan 430072, China*
[2]*School of Physics and Electronics, Hunan University, Changsha 410082, China*
[3]*School of Electronics and Information Engineering, Wuhan Donghu University, Wuhan 430212, China*

(Received 10 November 2017; revised manuscript received 17 October 2018; published 11 February 2019)

Width modulation has long been proven to be an effective method for band-gap engineering of graphene nanoribbons (GNRs). The success of bottom-up GNR synthesis technology has led to the realization of width modulation within a nanoribbon, which is regarded as a GNR heterojunction (HJ). However, the HJ "shape" does not guarantee an ideal HJ band structure. We report a first-principles investigation of GNR HJs composed of narrow and wide GNR segments. Two possible coupling modes exist when two GNR segments with different widths are connected. We find that the electronic states near the Fermi level are localized in the small band-gap segment for one coupling mode, whereas they are almost equally distributed in the two segments for the other one. Consequently, only the former mode can produce a HJ band structure. The underlying mechanisms are analyzed using two hypothetical experiments. The delocalized electronic states are generated by the interface edge C—C bonds. The stabilities of the two coupling modes are verified by molecular dynamics simulations. To exclude other factors and demonstrate the universality of this finding, GNR HJs with varied lengths and widths are also studied. These investigations provide insights into GNR HJ constructions.

DOI: 10.1103/PhysRevApplied.11.024026

I. INTRODUCTION

The remarkable width and edge control abilities of bottom-up graphene nanoribbon (GNR) synthesis technology have stimulated intense investigations into GNR preparation and characterization methods [1–7]. The fascinating characteristics of GNRs, including spin [8,9], magnetism [10], and doping [4,11], have long been investigated in great detail. Among the various geometrical structures of GNRs, the unique band-gap-width relationship [12,13] and fascinating transport properties [14] of armchair GNRs (aGNRs) allow them to outperform two-dimensional monolayer graphene in next-generation electronic materials [15,16]. Because of rapidly improved technology, GNR heterojunction (HJ) structures are regularly reported to possess good properties in quantum dot and optical applications. Early GNR intraribbon HJs were synthesized via controllable dehydrogenation at specific regions in the ribbons [17]. Recently, Cai *et al.* reported chevron-type GNR HJs made by partial doping [18]. The actual HJs made of wide and narrow GNR segments were first reported by Chen *et al.*, who synthesized a 7-13-7 aGNR HJ through a bottom-up method using pristine hydrocarbon precursors [19]. The authors observed spatially modulated electronic states and theoretically confirmed their existence by first-principles calculations. More recently, Wang *et al*. further studied the quantum dot effect using a 7-14-7 aGNR HJ [20]. Many GNR HJ applications rely on the hypothesis that the band gaps of the wide and narrow GNR segments are invariable after their connections, generating HJ band structures with band offsets in the interfaces [21–23]. However, in low-dimensional material-based HJs, ideal HJ band structures are easily destroyed by electronic state interactions between different segments [24]. Considering the similar planar hexagonal structures of the two sides of the GNR HJs, whether they can generate HJ band structures is still a matter of controversy.

Electronic state spatial localization is a prerequisite for the HJ band structure. In theoretical investigations, Sevinçli *et al.* studied a superlattice built by 5–7 aGNR HJs and observed localized states [25]. Surprisingly, the states of the valence band maximum (VBM) and the conduction band minimum (CBM) did not exhibit the localization phenomenon; as a result, no HJ band structure was established. The localization of the VBM and CBM was observed by Prezzi *et al*. in a 4.3-nm-long 7–8 aGNR HJ [26]. The authors also mentioned that the VBM and CBM would

*changsheng@whu.edu.cn

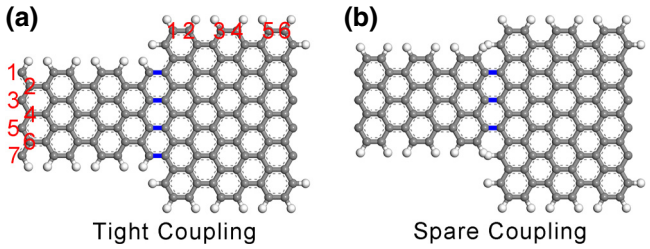

FIG. 1. Schematic illustrations of the TC (a) and SC (b) modes in the 7-13-6-6 GNR HJs. All the dangling bonds of C atoms are saturated by H atoms. The widths and lengths of the GNR segments are defined by their atom numbers in the corresponding directions, as shown in (a). There are four bonds connecting the 7- and 13-aGNR segments in the TC junction compared to only three in the SC junction.

no longer be localized if the HJ length was too short. However, in an 11–17 aGNR HJ with a length of only 10 atoms, state localization was still observed by Tong *et al.* [27]. Moreover, other recent studies also found the electronic state localization or quantum-well effect in GNR HJs and their derivatives [10,28,29]. These results suggest two interesting questions: Why is the electronic state localization strong in some HJs but weak in others, and how can we construct a functional GNR HJ with both HJ "shape" and band structures? To answer these questions, the coupling modes of the junction interfaces should be investigated [30,31].

In this work, based on first-principles simulations [32], GNR HJ interface connections are studied. Considering the nonzero band gaps and the feasibility in experiments [19, 33], the abrupt junctions consisting of perfect aGNR segments are investigated. When two aGNR segments with different widths are connected, there are two coupling modes (see Fig. 1) [30], both of which are stable structures. Conveniently, the couplings with more and fewer C—C bonds can be called tight and spare couplings (TCs and SCs), respectively. Note that the 7-aGNR edges are connected to the 13-aGNR in the TC HJ, while they are not in the SC HJ. For clear expression, the GNR HJs are referred to by their size: M-N-P-Q, where M and N are the widths of the narrow and wide aGNR segments, respectively, and P and Q are the corresponding lengths.

Simulation results demonstrate that the electronic states near Fermi levels are easily spatially localized to one segment in the SC HJs, while they are distributed uniformly in the TC HJs. Consequently, only the SC mode can generate HJ band structures with band offsets in the interfaces. The delocalized states in the TC HJs are mainly generated from the junction interface edges. Compared with other factors that can also induce state localization, the coupling mode is much more crucial and is a general rule for aGNR HJs.

II. METHODS

The Becke-Lee-Yang-Parr (BLYP) generalized gradient approximation (GGA) exchange-correlation function is employed in the ab initio calculations, and the pseudopotential is norm-conserving [34–37]. The underestimates of band gaps are not considered [11,38] because the band gaps of aGNRs would be reduced in a real environment [13,19,39]. Moreover, neglecting these underestimates does not influence the state localization analyses [26]. We use $1 \times 1 \times 10$ and $1 \times 1 \times 25$ k-point grids in the self-consistent and non-self-consistent electronic state calculations [9]. The kinetic energy cutoff of the wavefunctions is 544 eV, and the total energy convergence threshold is 1.4×10^{-5} eV [11,38,40]. Vacuum spaces of more than 10 Å are included in the width and thickness directions to minimize the interactions between the calculated HJs and their periodic images [20]. To avoid additional edge states, no vacuum layer is added in the length direction.

To verify the stabilities of the studied structures, Car-Parrinello molecular dynamics (MD) is also used [41]. The same exchange-correlation function and kinetic energy cutoff for the plane-wave basis are employed [42]. Only the Gamma point within the Brillouin zone is considered [43,44]. The convergence thresholds on the total energies and forces are 1.4×10^{-5} eV and 2.6×10^{-3} eV/Å, respectively [42,45]. Before MD, we compute the ground state wavefunctions via direct minimizations of the energy functions. The steepest descent (SD) and damped dynamic algorithms are used consecutively to reduce the total energies of the systems for 1.2×10^{-3} and 5.1×10^{-2} ps, respectively. The atom positions are fixed in these steps. Next, the systems are exposed to temperatures ranging from 100 to 1100 K with an interval of 200 K for 1.2 ps each [46,47]. Both the electron and ion dynamics are set to Verlet, and both the atomic positions and the supercells are varied. The Nose-Hoover thermostat controlling the ionic kinetic energies is adopted [48].

All the simulations above are carried out with the assistance of the open-source QUANTUM-ESPRESSO package [32,49].

III. RESULTS AND DISCUSSIONS

A. Electronic state spatial localization

The local densities of states (LDOS) of the 7-13-6-6 TC and SC HJs in k space are shown in Figs. 2(a) and 2(b). The total LDOS can be projected (PDOS) onto the narrow and wide ribbon segments. Only the p_z orbitals of C atoms are considered in the projections because the electronic properties of graphene are mainly controlled by the π electrons [33]. In each structure, the Fermi level is shifted to zero energy. The first valence and conduction bands (VB1 and CB1) are localized in the 13-aGNR segment of the

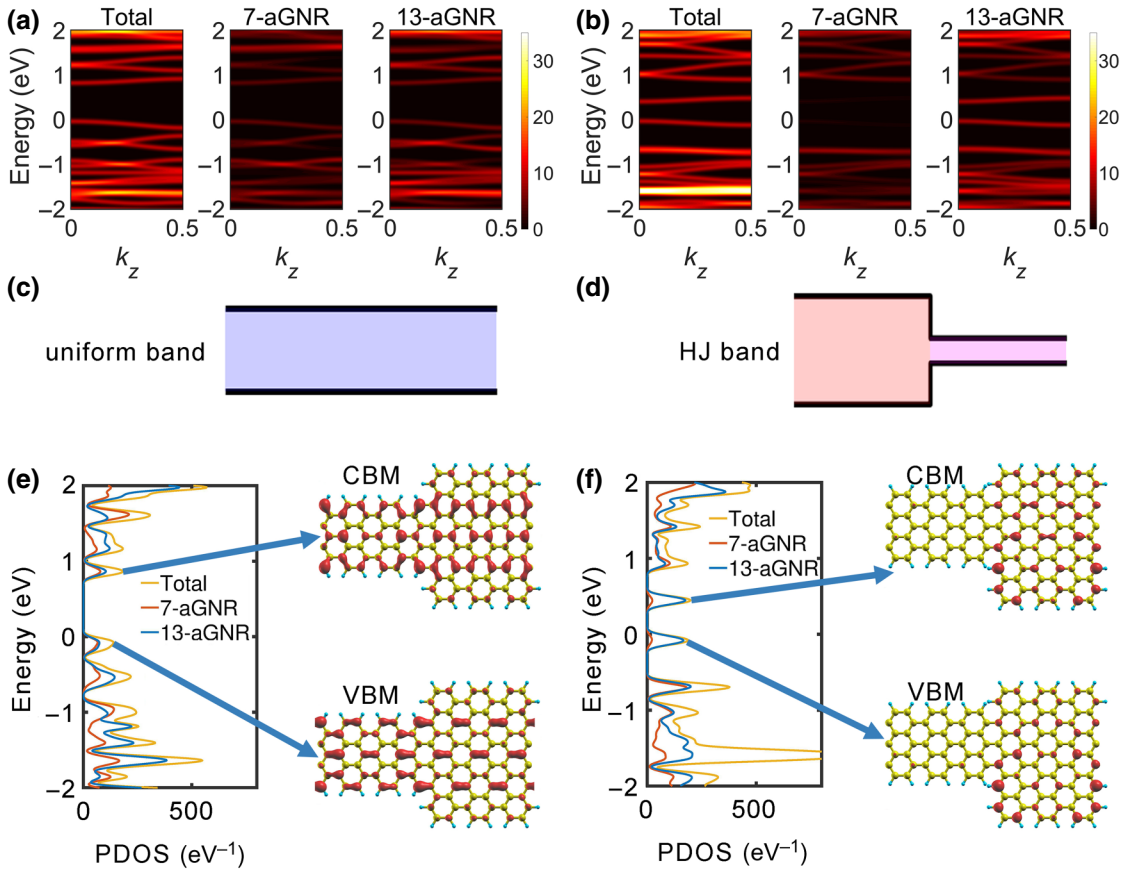

FIG. 2. *k*-space LDOS of the 7-13-6-6 TC (a) and SC (b) HJs. The LDOS can be separately projected to the 7- and 13-aGNR segments. It can be intuitively inferred from the PDOS that the band gaps of the 7- and 13-aGNR segments are the same in (a) and different in (b). Consequently, the uniform and HJ band structures are established, as illustrated in (c) and (d). The PDOS in energy space are also shown in (e) and (f). The real space distributions of the VBM and CBM are displayed on the right. The values of the isosurfaces are 10% of the maximum DOS. The uniform and HJ band structures are more clearly demonstrated.

SC HJ. The band gap of the 7-aGNR segment is 1.55 eV, which is very similar to that of the intact 7-aGNR [see Fig. 8(a) in the Appendix]. Compared to their intact counterparts, the band gap of the 13-aGNR segment is reduced. A type-I HJ band structure is observed, as illustrated in Fig. 2(d). In comparison, the electronic states in VB1 and CB1 are distributed throughout the whole structure in the TC HJ, leading to a uniform band gap of 0.86 eV, as illustrated in Fig. 2(c), identical to that of the intact 13-aGNR [see Fig. 8(b) in the Appendix].

The PDOS values in energy space can be found in Figs. 2(e) and 2(f). The PDOS proportion of the VB1 and CB1 in the 7-aGNR segment (the values of the orange lines and yellow lines in these subplots) is only approximately 10% in the SC HJ, whereas this value is nearly 50% in the TC HJ. A smaller value means greater electronic state localization, which is also intuitively shown in the states' real space distributions on the right. Consequently, the HJ band structure is generated by the SC HJ, whereas the TC HJ exhibits only a uniform band structure.

B. Localization and delocalization mechanisms

To determine the mechanisms controlling the electronic state spatial distributions in the TC-SC HJs, the origins of these states should first be confirmed. The uniform band gap in the 7-13-6-6 TC HJ is the same as that in the intact 13-aGNR. Thus, the VB1 and CB1 seem to be generated by the 13-aGNR segment. However, from the real space location plots of the VBM and CBM in Fig. 2(e), the VB1 and CB1 also seem to be generated by the 7-aGNR segment. A recent work has pointed out that they could be interface-state-derived bands [31]. To verify this viewpoint, a hypothetical strain-induced electronic state spatial redistribution experiment is conducted, as shown in Fig. 3. Local strains are induced in the width direction of the 13-aGNR segments to show the state transfers more clearly. This strain strategy has also previously been used in GNR HJ thermal resistance investigations [50].

When a −4% strain (compressive) is exerted on the TC HJ [Fig. 3(a)], the electronic states of the CB1 are pushed from the 7- to the 13-aGNR segment. When the strain

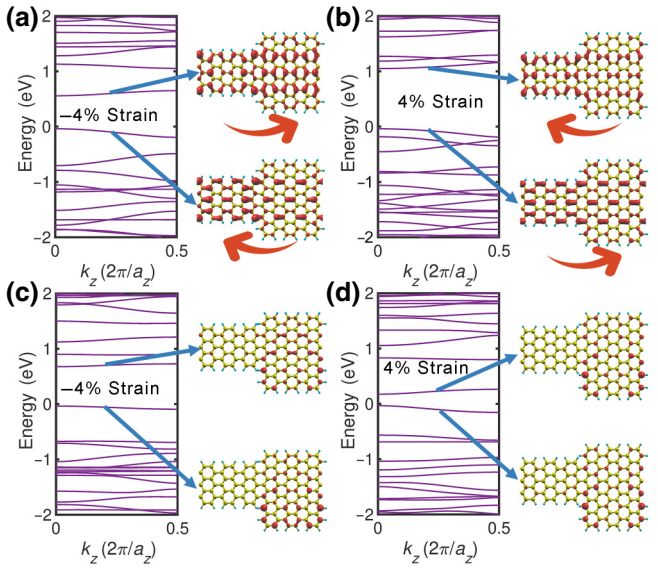

FIG. 3. State redistributions in the 7-13-6-6 TC (a) and (b) and SC (c) and (d) HJs under partial strains. The negative (compressive) and positive (tensile) strains along the width direction are exerted on the 13-aGNR segments. The values of the isosurfaces are 10% of the maximum DOS.

becomes 4% (tensile) [Fig. 3(b)], the states are pulled back again. Similar phenomena can also be observed in the electronic states of the VB1, albeit with an opposite trend. The electronic state redistributions are cross segmental, indicating that they do not initially belong to any segment. In contrast, the phenomena in the SC HJ are completely different. Regardless of the direction of the strains, the electronic states of the VB1 and CB1 always redistribute within the 13-aGNR segment. They are barely pushed to the 7-aGNR segment, indicating that they belong to the 13-aGNR segment. These observations are identical to the proposal that the VB1 and CB1 in the TC HJs are generated by the junction interfaces. Moreover, it can also be inferred that these bands in the SC HJs are generated by the small band-gap segments. The different origins cause different spatial distribution behaviors, thereby leading to different band-gap properties.

However, interfaces also exist in the SC HJs, and no interface state is observed near the Fermi levels. As mentioned above, the most obvious distinction between these two coupling modes is that the narrow segment edges are connected to the wide segment in the TC HJ. To more precisely locate the origin of the interface states, two hypothetical structures are further studied. They are obtained by removing the edge [Fig. 4(a)] and middle [Fig. 4(b)] C atoms in the connecting region of the 7-13-6-6 TC HJ. The positions without C atoms can be regarded as defects. Therefore, defect energy bands are generated in the band structures. As they commonly concentrate near defects, these energy bands can be distinguished by their real space

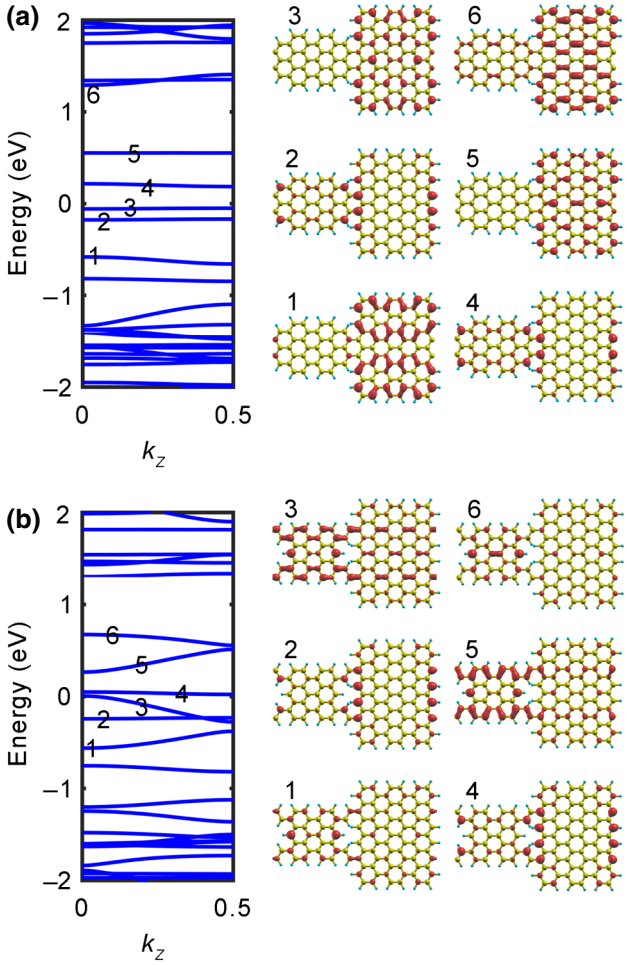

FIG. 4. Band structures of the 7-13-6-6 TC HJ without interface edge (a) and middle (b) atoms. The real space distributions of the bands near the Fermi levels are shown on the right. The values of the isosurfaces are 10% of the maximum DOS.

locations, such as band2 in the two subplots. Neglecting these bands, other bands in these two structures near the Fermi levels show different spatial distributions. Without the edge atoms, the interface states that are distributed in both segments are eliminated. However, they still exist when just the middle atoms are removed. The contrasting results imply that the interface states are mainly generated by the edges of the TC interfaces. This result is reasonable for aGNRs because their fundamental properties strongly depend on edges [33,51,52]. These conclusions can also help explain the delocalization of the CBM and VBM in the 5-7-6-6 TC junction superlattices studied in a previous work [25].

C. Stabilities

Since there are fewer C—C bonds connecting two different aGNR segments in the SC HJs than in the TC HJs, the stabilities of the two coupling modes should be studied. Therefore, the Car-Parrinello MD method is adopted to

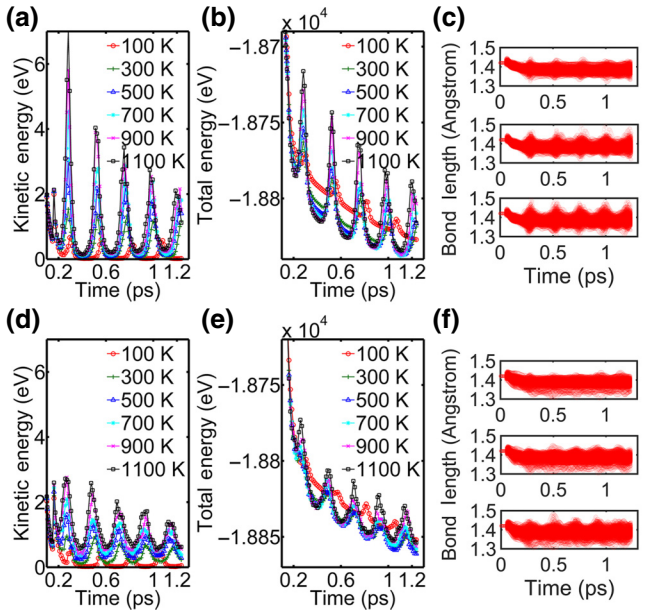

FIG. 5. Kinetic and total energies and C—C bond length variations of the 7-13-6-6 TC (a)–(c) and SC (d)–(f) HJs at different temperatures. In (e) and (f), the simulation temperatures are 300, 700, and 1100 K from the top to the bottom.

simulate and compare the behaviors of the two aGNR HJs at different temperatures (Fig. 5) [46]. Both the kinetic and total energies of the coupling modes exhibit periodicities. When the temperature increases, the energy fluctuations are also increased. Similar responses to temperatures are observed in the TC and SC HJs. Over time, the fluctuations are all gradually reduced, and the total energies are lowered. The C—C bond-length variations of the two HJs are depicted in Figs. 5(c) and 5(f). Clear periodicities in the length variations of the TC HJ are observed at different temperatures. In comparison, the bond lengths in the SC HJ fluctuate more obviously. The additional fluctuations are mainly induced by the interface edge atoms (see the red ellipses in Fig. 9 in the Appendix). However, these fluctuations are small and cannot induce structural instability. For example, at the end of the MD process at 300 K, the mean C—C bond length in the interface edges is only 0.03 Å shorter than the value in other regions. Compared with the bond lengths, this value is negligible. Furthermore, the empirical C—C bond cut-off distance is in the range from 1.92 to 2.00 Å [53], much larger than the simulated bond-length-variation ranges, demonstrating the stabilities of the SC HJs at different temperatures.

Additionally, to determine the electronic effects related to the distortions of the SC interface edges, the PDOS of the SC HJ after the MD process at 300 K are also calculated (see Fig. 10 in the Appendix). The distortions barely affect the localization, except for a few enhancements.

D. Size effect

Note that the amplitude of an electronic wavefunction will degenerate naturally when it diffuses across a HJ [54]. In GNR HJs, the degeneration can help localize wavefunctions of electronic states. The degree of localization will be enhanced with increased segment width differences and lengths [26]. From this perspective, the localization abilities of this natural degeneration phenomenon and the coupling modes should be compared.

First, the 7-13-*P*-*Q* TC and SC HJ families with increasing lengths are investigated. The lengths of the two segments are equal ($P = Q$). As mentioned above, for an energy band near the Fermi level, a smaller PDOS proportion in the large band-gap segment indicates greater localization behavior of this band. As a quantitative index, the PDOS proportions in the 7-aGNR segments of these HJs are calculated in Fig. 6. In addition to the VB1 and CB1, the second valence (VB2) and conduction (CB2) bands are also considered. In the TC HJs [Fig. 6(a)], the proportions of VB1 and CB1 decrease gradually along the segment length, which can be attributed to the natural degeneration phenomenon. For the VB2 and CB2, the reductions are even slower. When the length of the HJ reaches 5.96 nm, the proportions of all the considered bands are still larger than 20%, suggesting a weak localization ability induced by the natural degeneration phenomenon. This weak localization ability will generate obscure interfaces in the TC HJ energy bands [24], degrading the performance of the GNR HJ in many applications.

For the SC HJs [Fig. 6(b)], the localization of the VB1 and CB1 is strong from the beginning and remains stable as the segment length continues to increase. The PDOS proportions of the VB2 and CB2 in the 7-aGNR segments also decrease rapidly and reach less than 20% at the 5.96-nm HJ length. Comparisons between the TC and SC HJ families suggest that the coupling modes are much more crucial than the natural degeneration in electronic

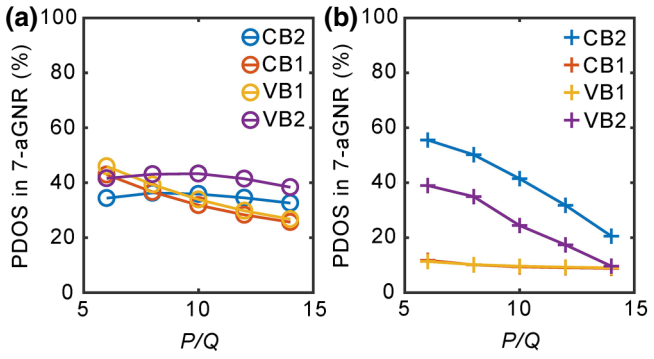

FIG. 6. PDOS proportions of the energy bands in the 7-aGNR segments of the 7-13-*P*-*Q* TC (a) and SC (b) HJ families. Here, *P* and *Q* are equal.

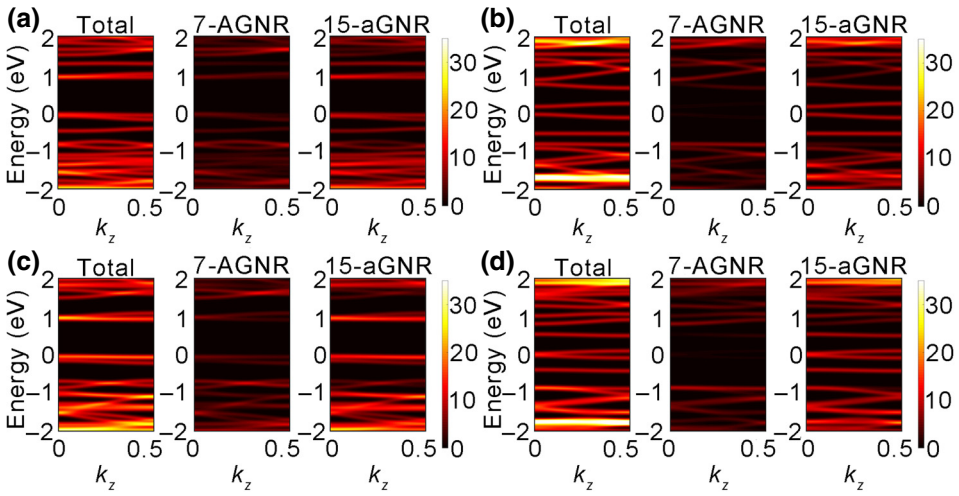

FIG. 7. *k*-space LDOS of the 7-15-6-6 TC (a) and SC (b) and 7-17-6-6 TC (c) and SC (d) HJs. The PDOS subplots of different segments are also shown.

state spatial localization. The SC mode is necessary for obtaining aGNR HJs with great performances.

Next, to further validate the universality of the localization behaviors of the two coupling modes, the PDOS of the 7-15-6-6 and 7-17-6-6 GNR TC and SC HJs in *k* space are also plotted in Fig. 7. Without exception, they all follow the rule that the electronic state spatial localization is more obvious in the SC HJs than in the TC HJs. The PDOS proportions of CB1 in the 7-aGNR segments are 11.76%, 10.51%, and 7.19% for the 7-13-6-6, 7-15-6-6, and 7-17-6-6 SC HJs, respectively. The slight decrease in PDOS proportion is also attributed to the natural degeneration phenomenon, which has a less obvious effect than the coupling modes.

In addition, it is noted that the 7-13-6-6 GNR TC HJ is symmetric in the width direction (see Fig. 11 in the Appendix). However, the symmetry is broken when it is changed to a SC HJ. One may consider the effect of symmetry on state localization; however, the 7-15-6-6 GNR HJ indicates that this effect can be excluded, as the coupling mode of its symmetric structure is SC, opposite to that of the 7-13-6-6 GNR HJ. Nevertheless, the localization behaviors of the SC and TC modes are similar in these two GNR HJs, indicating a weak relation between symmetry and localization.

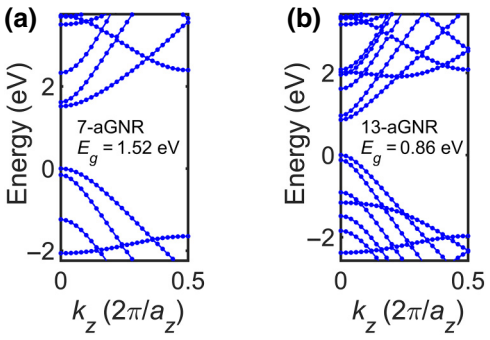

FIG. 8. Band structures of the 7- (a) and 13-aGNR (b).

IV. CONCLUSIONS

We demonstrate the crucial effect of the coupling modes on electronic state spatial localization in GNR HJs built by narrow-wide GNR combinations. In the SC HJs, the states near the Fermi levels are generated by the small band-gap segments. Therefore, they can be well localized in these segments. In contrast, the states near the Fermi levels in the TC HJs are distributed throughout the whole structures since they are generated by the junction interfaces. The stabilities of these two coupling modes are verified by MD simulations and their localization behaviors with variations in the HJ length and width are further studied. We show that the SC mode is more favorable than the TC mode in GNR HJ constructions, which can be regarded as a design rule. Moreover, many applications, such as tunneling and photovoltaics devices, rely on the

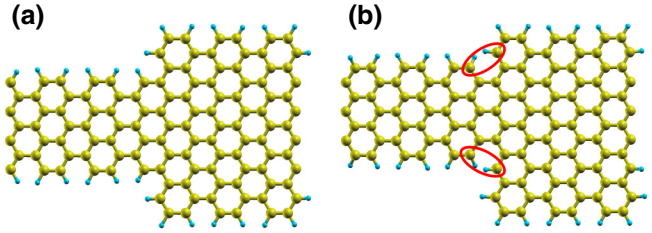

FIG. 9. Structures of the 7-13-6-6 TC (a) and SC (b) HJs after Car-Parrinello MD simulations at 300 K. The atomic displacements in the SC HJ are more obvious than those in the TC HJ because of the repulsive forces between the closed H atoms indicated by red ellipses. The closed H atoms are removed from the GNR plane and induce some displacements on the nearest C atoms.

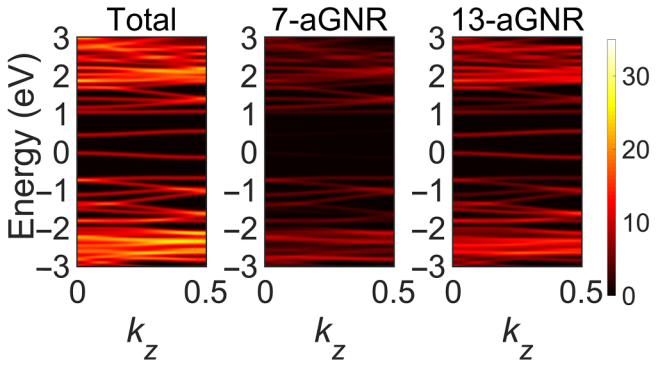

FIG. 10. PDOS in the 7- and 13-aGNR segments of the 7-13-6-6 SC HJ after Car-Parrinello MD simulations.

HJ band structures. This rule can provide guidance for their realizations and improvements.

ACKNOWLEDGMENTS

This work was supported by the National Natural Science Foundation of China (Grants No. 61404094, No. 61574102 and No. 61774113), the Fundamental Research Fund for the Central Universities, Wuhan University (Grants No. 2042016kf0189 and No. 2042017gf0052), the China Postdoctoral Science Foundation (Grant No. 2012T50688) and the Natural Science Foundation of Hubei Province, China (Grant No. 2017CFB660).

APPENDIX

Figure 8 shows the band structures of 7- and 13-aGNRs; Fig. 9 shows the structures of 7-13-6-6 GNR HJs after MD simulation at 300 K, and the PDOS plot is depicted in Fig. 10; Fig. 11 illustrates the symmetries of the GNR HJs.

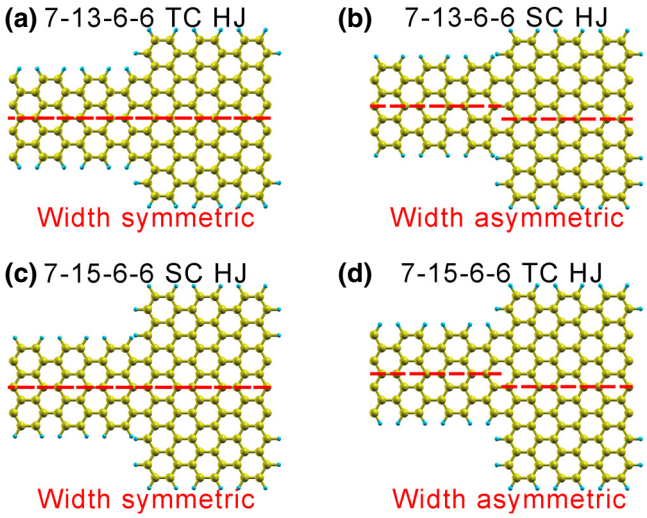

FIG. 11. Schematic illustrations of the width symmetric and asymmetric GNR HJs.

[1] J. Cai, P. Ruffieux, R. Jaafar, M. Bieri, T. Braun, S. Blankenburg, M. Muoth, A. P. Seitsonen, M. Saleh, X. Feng, K. Mullen, and R. Fasel, Atomically precise bottom-up fabrication of graphene nanoribbons, Nature **466**, 470 (2010).

[2] S. Linden, D. Zhong, A. Timmer, N. Aghdassi, J. H. Franke, H. Zhang, X. Feng, K. Mullen, H. Fuchs, L. Chi, and H. Zacharias, Electronic Structure of Spatially Aligned Graphene Nanoribbons on Au(788), Phys. Rev. Lett. **108**, 216801 (2012).

[3] Y.-C. Chen, D. G. de Oteyza, Z. Pedramrazi, C. Chen, F. R. Fischer, and M. F. Crommie, Tuning the band gap of graphene nanoribbons synthesized from molecular precursors, ACS Nano **7**, 6123 (2013).

[4] T. H. Vo, M. Shekhirev, D. A. Kunkel, F. Orange, M. J. F. Guinel, A. Enders, and A. Sinitskii, Bottom-up solution synthesis of narrow nitrogen-doped graphene nanoribbons, Chem. Commun. **50**, 4172 (2014).

[5] C. Sanchez-Sanchez, T. Dienel, O. Deniz, P. Ruffieux, R. Berger, X. Feng, K. Mullen, and R. Fasel, Purely armchair or partially chiral: Noncontact atomic force microscopy characterization of dibromo-bianthryl-based graphene nanoribbons grown on Cu(111), ACS Nano **10**, 8006 (2016).

[6] H. Hayashi, J. Yamaguchi, H. Jippo, R. Hayashi, N. Aratani, M. Ohfuchi, S. Sato, and H. Yamada, Experimental and theoretical investigations of surface-assisted graphene nanoribbon synthesis featuring carbon–fluorine bond cleavage, ACS Nano **11**, 6204 (2017).

[7] A. Basagni, F. Sedona, C. A. Pignedoli, M. Cattelan, L. Nicolas, M. Casarin, and M. Sambi, Molecules-oligomers-nanowires-graphene nanoribbons: A bottom-up stepwise on-surface covalent synthesis preserving long-range order, J. Am. Chem. Soc. **137**, 1802 (2015).

[8] A. R. Botello-Méndez, E. Cruz-Silva, F. López-Urías, B. G. Sumpter, V. Meunier, M. Terrones, and H. Terrones, Spin polarized conductance in hybrid graphene nanoribbons using 5−7 defects, ACS Nano **3**, 3606 (2009).

[9] P. Cui, J. H. Choi, W. Chen, J. Zeng, C. K. Shih, Z. Li, and Z. Zhang, Contrasting structural reconstructions, electronic properties, and magnetic orderings along different edges of zigzag transition metal dichalcogenide nanoribbons, Nano Lett. **17**, 1097 (2017).

[10] D. Wang, Z. H. Zhang, X. Q. Deng, Z. Q. Fan, and G. P. Tang, Magnetism and magnetic transport properties of the polycrystalline graphene nanoribbon heterojunctions, Carbon **98**, 204 (2016).

[11] Y.-F. Zhang, Y. Zhang, G. Li, J. Lu, Y. Que, H. Chen, R. Berger, X. Feng, K. Müllen, X. Lin, Y.-Y. Zhang, S. Du, S. T. Pantelides, and H.-J. Gao, Sulfur-doped graphene nanoribbons with a sequence of distinct band gaps, Nano Res. **10**, 3377 (2017).

[12] P. Ruffieux, J. Cai, N. C. Plumb, L. Patthey, D. Prezzi, A. Ferretti, E. Molinari, X. Feng, K. Müllen, C. A. Pignedoli, and R. Fasel, Electronic structure of atomically precise graphene nanoribbons, ACS Nano **6**, 6930 (2012).

[13] H. Huang, D. Wei, J. Sun, S. L. Wong, Y. P. Feng, A. H. Neto, and A. T. Wee, Spatially resolved electronic

structures of atomically precise armchair graphene nanoribbons, Sci. Rep. **2**, 983 (2012).
[14] P. B. Bennett, Z. Pedramrazi, A. Madani, Y.-C. Chen, D. G. de Oteyza, C. Chen, F. R. Fischer, M. F. Crommie, and J. Bokor, Bottom-up graphene nanoribbon field-effect transistors, Appl. Phys. Lett. **103**, 253114 (2013).
[15] V. Meunier, A. G. Souza Filho, E. B. Barros, and M. S. Dresselhaus, Physical properties of low-dimensionalsp2-based carbon nanostructures, Rev. Mod. Phys. **88**, 025005 (2016).
[16] X. Li, L. Tao, Z. Chen, H. Fang, X. Li, X. Wang, J.-B. Xu, and H. Zhu, Graphene and related two-dimensional materials: Structure-property relationships for electronics and optoelectronics, Appl. Phys. Rev. **4**, 021306 (2017).
[17] S. Blankenburg, J. Cai, P. Ruffieux, R. Jaafar, D. Passerone, X. Feng, K. Müllen, R. Fasel, and C. A. Pignedoli, Intraribbon heterojunction formation in ultranarrow graphene nanoribbons, ACS Nano **6**, 2020 (2012).
[18] J. Cai, C. A. Pignedoli, L. Talirz, P. Ruffieux, H. Sode, L. Liang, V. Meunier, R. Berger, R. Li, X. Feng, K. Mullen, and R. Fasel, Graphene nanoribbon heterojunctions, Nat. Nanotechnol. **9**, 896 (2014).
[19] Y. C. Chen, T. Cao, C. Chen, Z. Pedramrazi, D. Haberer, D. G. de Oteyza, F. R. Fischer, S. G. Louie, and M. F. Crommie, Molecular bandgap engineering of bottom-up synthesized graphene nanoribbon heterojunctions, Nat. Nanotechnol. **10**, 156 (2015).
[20] S. Wang, N. Kharche, E. Costa Girao, X. Feng, K. Mullen, V. Meunier, R. Fasel, and P. Ruffieux, Quantum dots in graphene nanoribbons, Nano Lett. **17**, 4277 (2017).
[21] L. Kai-Tak, S. Dawei, C. Sai-Kong, S. Bala Kumar, G. Samudra, Y. Yee-Chia, and G. Liang, A simulation study of graphene-nanoribbon tunneling FET with heterojunction channel, IEEE Electron Dev. Lett. **31**, 555 (2010).
[22] Y. Lv, Q. Huang, H. Wang, S. Chang, and J. He, A numerical study on graphene nanoribbon heterojunction dual-material gate tunnel FET, IEEE Electron Device Lett. **37**, 1354 (2016).
[23] A. M. M. Hamam, M. E. Schmidt, M. Muruganathan, S. Suzuki, and H. Mizuta, Sub-10 nm graphene nano-ribbon tunnel field-effect transistor, Carbon **126**, 588 (2018).
[24] C. Zhang, Y. Chen, J. K. Huang, X. Wu, L. J. Li, W. Yao, J. Tersoff, and C. K. Shih, Visualizing band offsets and edge states in bilayer-monolayer transition metal dichalcogenides lateral heterojunction, Nat. Commun. **6**, 10349 (2016).
[25] H. Sevinçli, M. Topsakal, and S. Ciraci, Superlattice structures of graphene-based armchair nanoribbons, Phys. Rev. B **78**, 245402 (2008).
[26] D. Prezzi, D. Varsano, A. Ruini, and E. Molinari, Quantum dot states and optical excitations of edge-modulated graphene nanoribbons, Phys. Rev. B **84**, 041401 (2011).
[27] H. Tong and M. W. Wu, Strongly modulated transmissions in gapped armchair graphene nanoribbons with side-arm or on-site gate voltage, Phys. Rev. B **85**, 205433 (2012).
[28] K. P. Dou, X. X. Fu, A. De Sarkar, and R. Q. Zhang, Tailoring the transmission lineshape spectrum of zigzag graphene nanoribbon based heterojunctions via controlling their width and edge protrusions, Nanoscale **7**, 20003 (2015).
[29] W. Zhang, C. Basaran, and T. Ragab, Impact of geometry on transport properties of armchair graphene nanoribbon heterojunction, Carbon **124**, 422 (2017).
[30] T. Cao, F. Zhao, and S. G. Louie, Topological Phases in Graphene Nanoribbons: Junction States, Spin Centers, and Quantum Spin Chains, Phys. Rev. Lett. **119**, 076401 (2017).
[31] D. J. Rizzo, G. Veber, T. Cao, C. Bronner, T. Chen, F. Zhao, H. Rodriguez, S. G. Louie, M. F. Crommie, and F. R. Fischer, Topological band engineering of graphene nanoribbons, Nature **560**, 204 (2018).
[32] P. Giannozzi *et al.*, QUANTUM ESPRESSO: A modular and open-source software project for quantum simulations of materials, J. Phys.: Condens. Matter **21**, 395502 (2009).
[33] Y.-W. Son, M. L. Cohen, and S. G. Louie, Energy Gaps in Graphene Nanoribbons, Phys. Rev. Lett. **97**, 216803 (2006).
[34] S. Goedecker, M. Teter, and J. Hutter, Separable dual-space Gaussian pseudopotentials, Phys. Rev. B **54**, 1703 (1996).
[35] C. Hartwigsen, S. Goedecker, and J. Hutter, Relativistic separable dual-space Gaussian pseudopotentials from H to Rn, Phys. Rev. B **58**, 3641 (1998).
[36] M. K. Kostov, E. E. Santiso, A. M. George, K. E. Gubbins, and M. B. Nardelli, Dissociation of Water on Defective Carbon Substrates, Phys. Rev. Lett. **95**, 136105 (2005).
[37] V. Tozzini and V. Pellegrini, Electronic structure and Peierls instability in graphene nanoribbons sculpted in graphane, Phys. Rev. B **81**, 113404 (2010).
[38] Y. Lv, S. Chang, H. Wang, J. He, and Q. Huang, Energy gap tunable graphene antidot nanoribbon MOSFET: A uniform multiscale analysis from band structure to transport properties, Carbon **101**, 143 (2016).
[39] N. Kharche and V. Meunier, Width and crystal orientation dependent band gap renormalization in substrate-supported graphene nanoribbons, J. Phys. Chem. Lett. **7**, 1526 (2016).
[40] Z. Lin, W. Qin, J. Zeng, W. Chen, P. Cui, J. H. Cho, Z. Qiao, and Z. Zhang, Competing gap opening mechanisms of monolayer graphene and graphene nanoribbons on strong topological insulators, Nano Lett. **17**, 4013 (2017).
[41] R. Car and M. Parrinello, Unified Approach for Molecular Dynamics and Density-Functional Theory, Phys. Rev. Lett. **55**, 2471 (1985).
[42] R. Zhao, J. Zhuang, Z. Liang, T. Yan, and F. Ding, The formation mechanism of multiple vacancies and amorphous graphene under electron irradiation, Nanoscale **7**, 8315 (2015).
[43] P. Rubio-Pereda and N. Takeuchi, Density functional theory study of the organic functionalization of hydrogenated graphene, J. Phys. Chem. C **117**, 18738 (2013).
[44] E. Menéndez-Proupin, P. Giannozzi, J. Peralta, and G. Gutiérrez, Ab initiomolecular dynamics study of amorphousCdTeOxalloys: Structural properties, Phys. Rev. B **79**, 014205 (2009).
[45] A. Tilocca and N. H. de Leeuw, Structural and electronic properties of modified sodium and soda-lime silicate glasses by Car–Parrinello molecular dynamics, J. Mater. Chem. **16**, 1950 (2006).
[46] B. Wang, S. Yuan, Y. Li, L. Shi, and J. Wang, A new Dirac cone material: A graphene-like Be3C2 monolayer, Nanoscale **9**, 5577 (2017).

[47] Z. Wang, Y. G. Zhou, J. Bang, M. P. Prange, S. B. Zhang, and F. Gao, Modification of defect structures in graphene by electron irradiation: Ab initio molecular dynamics simulations, J. Phys. Chem. C **116**, 16070 (2012).

[48] G. Cicero, A. Calzolari, S. Corni, and A. Catellani, Anomalous wetting layer at the Au(111) surface, J. Phys. Chem. Lett. **2**, 2582 (2011).

[49] C.-K. Skylaris, A benchmark for materials simulation, Science **351**, 1394 (2016).

[50] Y. Xue, Y. Chen, K. Cai, Z.-Y. Liu, Y. Zhang, and N. Wei, Local strain field engineering on interfacial thermal resistance of graphene nanoribbon, Appl. Phys. Lett. **112**, 021604 (2018).

[51] V. Barone, O. Hod, and G. E. Scuseria, Electronic structure and stability of semiconducting graphene nanoribbons, Nano Lett. **6**, 2748 (2006).

[52] R. Gillen, M. Mohr, C. Thomsen, and J. Maultzsch, Vibrational properties of graphene nanoribbons by first-principles calculations, Phys. Rev. B **80**, 155418 (2009).

[53] L. He, S. Guo, J. Lei, Z. Sha, and Z. Liu, The effect of Stone–Thrower–Wales defects on mechanical properties of graphene sheets – A molecular dynamics study, Carbon **75**, 124 (2014).

[54] R. Tamura and M. Tsukada, Electronic transport in carbon nanotube junctions, Solid State Commun. **101**, 601 (1997).